

Cite this: *Mater. Adv.*, 2025,  
6, 1685Received 10th January 2025,  
Accepted 26th January 2025

DOI: 10.1039/d5ma00022j

rsc.li/materials-advances

# Type I and type II superconductivity in a quasi-2D Dirac metal†

Chris J. Lygouras,<sup>id</sup>\*<sup>a</sup> Junyi Zhang,<sup>id</sup><sup>a</sup> Jonah Gautreau,<sup>b</sup> Mathew Pula,<sup>b</sup> Sudarshan Sharma,<sup>id</sup><sup>b</sup> Shiyuan Gao,<sup>ac</sup> Tanya Berry,<sup>id</sup><sup>ac</sup> Thomas Halloran,<sup>a</sup> Peter Orban,<sup>a</sup> Gael Grissonnanche,<sup>de</sup> Juan R. Chamorro,<sup>ac</sup> Taketora Mikuri,<sup>f</sup> Dilip K. Bhoi,<sup>f</sup> Maxime A. Siegler,<sup>c</sup> Kenneth J.T. Livi,<sup>m</sup> Yoshiya Uwatoko,<sup>f</sup> Satoru Nakatsuji,<sup>afghij</sup> B. J. Ramshaw,<sup>dj</sup> Yi Li,<sup>a</sup> Graeme M. Luke,<sup>id</sup><sup>bk</sup> Collin L. Broholm<sup>alm</sup> and Tyrel M. McQueen<sup>id</sup><sup>acm</sup>

We explore bulk superconducting phase in single crystals of the Dirac material LaCuSb<sub>2</sub> prepared by the self-flux method. Magnetization, muon spin relaxation measurements, and density functional theory, show the Dirac nodal line Fermi surfaces give rise to type-II superconductivity for magnetic fields applied along the **a**-axis, and type-I superconductivity for fields along the **c**-axis. Both chemical and hydrostatic pressure drastically suppress the superconducting transition. We find multiband superconductivity evidenced by a precipitous drop in the electronic specific heat capacity and high-pressure susceptibility for  $T^* < T_c/3$ . Our work demonstrates dirty-limit, weak-coupling multiband superconductivity in LaCuSb<sub>2</sub>, and highlights the role of Dirac fermions on its anisotropic character.

## 1 Introduction

In topological semimetals, the electronic band structure features relativistic linearly-dispersive band crossings. This degeneracy gives rise to quasiparticles in condensed matter systems known as Dirac or Weyl fermions, analogous to those found in quantum

field theory. Realizing these in bulk materials is an exciting prospect because they bring about topological protection, physical properties beyond those seen in the semiclassical regime, and novel phases of matter. For example, Dirac semimetals are often found to have large linear transverse magnetoresistance, and negative longitudinal magnetoresistance, which are associated with a chiral anomaly in the underlying field theory.<sup>1,2</sup> New phases of matter can be realized when these topological fermions influence other electronic or magnetic properties, and *vice-versa*. Exotic topological phases like a monopole superconductor are predicted to arise in superconducting magnetic Weyl semimetals with inversion symmetry, whose gap functions are nodal and described by monopole harmonics.<sup>3</sup> On the way to realizing such novel classes of superconductors, it is natural to study centrosymmetric, non-magnetic superconductors that harbor Dirac fermions to understand the physical phenomena that emerge. One family of interest is the set of square-net materials that contain pnictogens like Sb or Bi, where Dirac fermions arise due to nonsymmorphic symmetry.<sup>4,5</sup> Chamorro *et al.*<sup>6</sup> found a large linear magnetoresistance and small effective masses in the square-net material LaCuSb<sub>2</sub> that were attributed to Dirac fermions. Earlier reports of superconductivity<sup>7,8</sup> in this material make it an ideal system to study the interplay between Dirac fermions and superconductivity, however superconductivity was not detected by Chamorro *et al.*

Here we resolve this contradiction, demonstrating that there is an extreme sensitivity of the physical properties to copper stoichiometry in LaCuSb<sub>2</sub>. We have grown single crystals of

<sup>a</sup> Institute for Quantum Matter and William H. Miller III Department of Physics and Astronomy, Johns Hopkins University, Baltimore, Maryland 21218, USA.

E-mail: clygour1@jhu.edu

<sup>b</sup> Department of Physics and Astronomy, McMaster University, Hamilton, Ontario, L8S 4M1, Canada

<sup>c</sup> Department of Chemistry, Johns Hopkins University, Baltimore, Maryland, 21218, USA

<sup>d</sup> Laboratory of Atomic and Solid State Physics, Cornell University, Ithaca, NY, USA

<sup>e</sup> Kavli Institute for Nanoscale Science, Ithaca, NY, USA

<sup>f</sup> Institute for Solid State Physics (ISSP), University of Tokyo, Kashiwa, Chiba, 277-8581, Japan

<sup>g</sup> Department of Physics, University of Tokyo, Bunkyo-ku, Tokyo 113-0033, Japan

<sup>h</sup> Trans-scale Quantum Science Institute, University of Tokyo, Bunkyo-ku, Tokyo 113-8654, Japan

<sup>i</sup> CREST, Japan Science and Technology Agency (JST), 4-1-8 Honcho Kawaguchi, Saitama, 332-0012, Japan

<sup>j</sup> Canadian Institute for Advanced Research, Toronto, M5G 1Z7, ON, Canada

<sup>k</sup> TRIUMF, Vancouver, British Columbia, V6T 2A3, Canada

<sup>l</sup> NIST Center for Neutron Research, National Institute of Standards and Technology, Gaithersburg, Maryland, 20899, USA

<sup>m</sup> Department of Materials Science and Engineering, Johns Hopkins University, Baltimore, Maryland, 21218, USA

† Electronic supplementary information (ESI) available. See DOI: <https://doi.org/10.1039/d5ma00022j>



LaCuSb<sub>2</sub> with varying copper content to study the effect of disorder on the superconducting state. In optimized samples with the highest superconducting  $T_c$  and closest to ideal stoichiometry, we used specific heat, susceptibility, magnetization, and muon spin rotation and relaxation ( $\mu$ SR) to characterize the highly anisotropic superconducting state. We utilize a combination of simple free-electron models, Bardeen–Cooper–Schrieffer (BCS) models, and tight-binding models to understand the fragile and anisotropic superconductivity in LaCuSb<sub>2</sub>.

## 2 Results

### 2.1 Structure

LaCuSb<sub>2</sub> crystallizes in the centrosymmetric, nonsymmorphic tetragonal space group  $P4/nmm$  (129). It can support both the Cu-deficient ZrCuSiAs structure,<sup>9,10</sup> and the Cu-excess defect-CaBe<sub>2</sub>Ge<sub>2</sub> structure, which features an interstitial Cu site<sup>10,11</sup> (Fig. 1a). We used  $N_{\text{Cu}}$ , related to the flux ratio used for crystal growth, as a parameter to tune stoichiometry in LaCuSb<sub>2</sub> and powder X-ray diffraction (XRD) to monitor the lattice constants of the resulting crystals (see methods). Fig. 1b shows the space

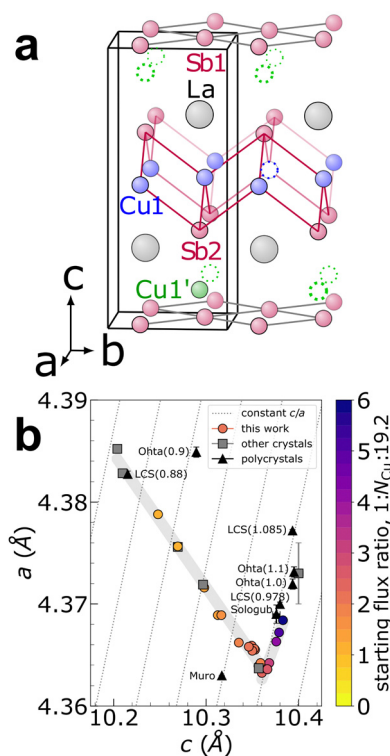


**Fig. 1** Structure and stoichiometry of LaCuSb<sub>2</sub>. (a) Crystal structure of LaCuSb<sub>2</sub>, showing the layered structure and square-net layers of Sb1. The sites Cu1 suffer from partial vacancy, and Cu1' suffer from partial occupancy. (b) Lattice constants  $a, c$  determined from powder X-ray diffraction, for various single crystals and polycrystalline samples from this work and from other works. Lines of constant  $c/a$  are used to compare samples in the literature. 'LCS( $X$ )' refer to polycrystal samples from this work, and their refined Cu occupancy  $X$  from powder XRD. Data from Muro *et al.*,<sup>8</sup> Sologub *et al.*<sup>9</sup> and Ohta<sup>10</sup> are indicated. Solid grey lines are derived from fitting the data to linear trendlines.

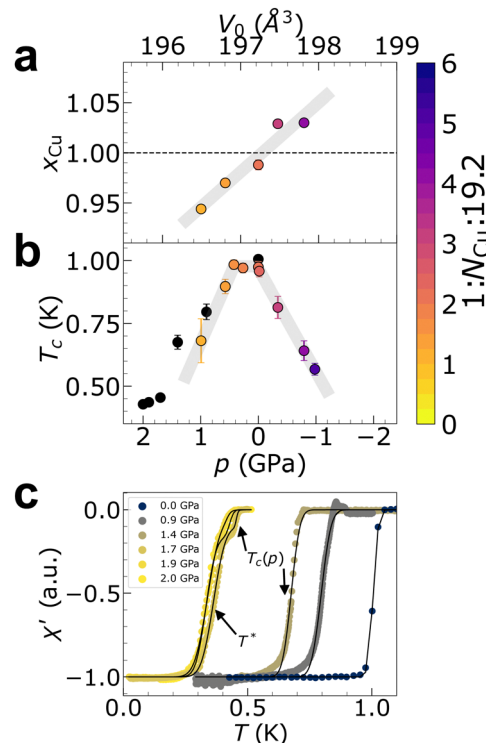


**Fig. 2** Dependence of physical properties on chemical and hydrostatic pressure in LaCuSb<sub>2</sub>. (a) Refined copper occupancy  $x_{\text{Cu}}$  derived from single-crystal XRD, versus room-temperature unit cell volume  $V_0 = ca^2$  derived from powder XRD. (b) Superconducting dome derived from magnetization measurements, showing the measured midpoint  $T_c$  versus  $V_0$  at ambient pressure, along with measured midpoint  $T_c$  versus hydrostatic pressure  $p$  for the optimized sample (black), the latter of which has refined occupancy  $x_{\text{Cu}} = 0.988(5)$ . Solid grey lines are fits to the data with linear trendlines. (c) Real part of the AC susceptibility for LaCuSb<sub>2</sub> under hydrostatic pressure. The transition  $T_c$  is seen to decrease and there appears to be a double-peak feature near  $T_c(p)$  and  $T^* \approx 0.35$  K at higher pressures. Solid lines are fits to the data using eqn (S4) (ESI†).

of lattice parameters  $a$  versus  $c$  (in Å) for various crystals at room temperature. There is a clear nearly-linear trend in the  $a$  versus  $c$  data below and above  $N_{\text{Cu}} \approx 2.25$ , where the trend changes from expanding  $c$ , contracting  $a$  to both expanding  $a$  and  $c$ . This is consistent with data from Ohta,<sup>10</sup> whereby the change in the lattice trends occurs at the change between Cu-deficient samples and Cu-excess samples. In the same plot, we have included data from crystals grown with differing starting flux ratios than that reported in this paper. These fall on roughly the same trendlines, affirming that the single parameter  $N_{\text{Cu}}$  can be used to tune a wide range of stoichiometry. We used single-crystal XRD to provide a quantitative estimate of the ratio of the elements, and in particular the copper concentration  $x_{\text{Cu}}$ , in various samples, as shown in Fig. 2a.

### 2.2 Superconducting dome

To demonstrate the effect of off-stoichiometry on the superconductivity, we measured DC magnetization on multiple samples grown with different flux ratios. We plotted  $T_c$  against parameters characterizing the sample that, over the relevant



range of stoichiometry, can be expected to vary if not in proportion then monotonically with the chemical potential. This is a self-doping process with Cu1 vacancies in the ZrCuSiAs structure for  $N_{\text{Cu}} \approx 2$  versus fully occupied Cu1 with interstitial Cu1' ions in the defect-CaBe<sub>2</sub>Ge<sub>2</sub> structure for  $N_{\text{Cu}} \approx 2$ . Both the unit cell volume  $V_0$  and the refined copper occupancy  $x_{\text{Cu}}$  are suitable parameters as a function of which to trace out the superconducting dome. The results are shown in Fig. 2a and b, while the supporting susceptibility data are shown in Fig. S2 and S3 (ESI<sup>†</sup>). We indeed see a systematic change in the superconducting transition temperature as a function of the unit cell and the Cu-occupancy. There is a nearly-linear increase of  $T_c$  at small unit cell volumes (Cu-deficient samples), a saturation near nominal stoichiometry until  $N_{\text{Cu}} \approx 2$ , and a nearly-linear decrease with larger unit cell volumes (Cu-excess samples).

### 2.3 Hydrostatic pressure

Given the large variation in the superconducting transition with chemical composition, we studied the effects of hydrostatic pressure on the superconducting state. As shown in Fig. 2c,  $T_c$  decreases with increasing pressures though full diamagnetic screening is achieved up to the largest pressure of 2 GPa accessed. The reduction in  $T_c$  with pressure amounts to  $dT_c/dp = -0.31(3)$  K GPa<sup>-1</sup>. The suppression of  $T_c$  with doping also occurs as the volume decreases at a rate  $dT_c/dv|_{\text{chem}} = 80(20)$  K, where  $dv = (V - V_0)/V_0$  relative to the optimized  $N_{\text{Cu}} = 2$ . If the effect of doping were solely associated with chemical pressure, then the corresponding bulk modulus  $K = -dT_c/dv|_{\text{chem}}(dT_c/dp)^{-1} = 270(80)$  GPa. With this, the extracted  $T_c$  and pressure can be directly compared to the chemical doping, as seen in Fig. 2b. Note the large effective bulk modulus may be taken as an indication that the effects of copper doping go beyond chemical pressure. Interestingly, for pressures between 1.7 GPa and 2 GPa, there is an anomaly within the transition to diamagnetism near  $T^* \approx 0.35$  K. The ambient-pressure specific heat capacity displays a potentially related second lower temperature anomaly near this temperature.

### 2.4 Specific heat capacity

To determine whether superconductivity is a bulk effect in LaCuSb<sub>2</sub> and glean information about the superconducting gap function, we turn to specific heat capacity measurements. For a stoichiometric sample in zero field,  $C_p/T$  features a sharp jump with midpoint  $T_c = 0.98(2)$  K (Fig. 3a). Apart from a higher transition temperature,  $C_p(T)$  is similar to that of polycrystalline samples reported by Muro *et al.*<sup>8</sup> Single crystalline samples, however, enable measurements with a well-defined field orientation. Our measurements of  $C_p(T)$  for fields applied along the *c*-axis are in Fig. 3a. For  $H = 75$  Oe superconductivity is fully suppressed, while for  $H = 25$  Oe the specific heat jump  $\Delta C_p$  at  $T_c = 0.81(4)$  K is actually enhanced over the zero field data, where  $\Delta C_p(T_c)/C_p(T_c) = 1.16(3)$  in 25 Oe compared with  $\Delta C_p(T_c)/C_p(T_c) = 0.94(4)$  in zero field.

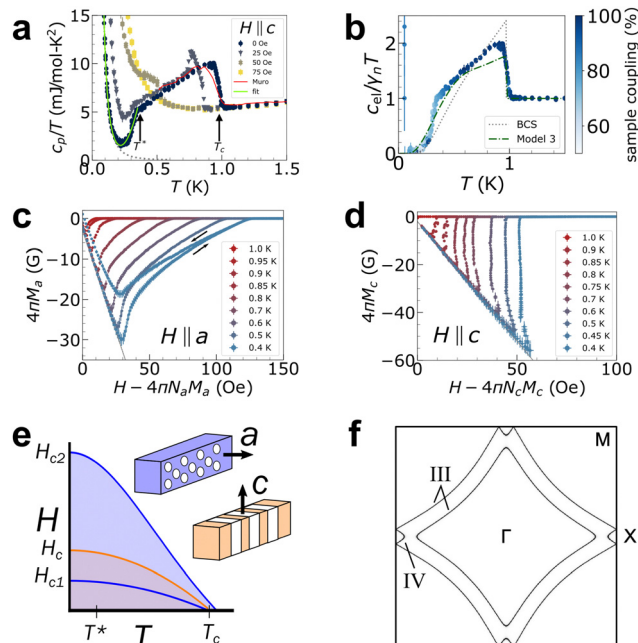


Fig. 3 Thermodynamics of the superconducting state of LaCuSb<sub>2</sub>. (a) Total specific heat  $C_p/T$  in applied magnetic field parallel to the *c*-axis. The superconducting transition temperature  $T_c$  and low-temperature anomaly  $T^*$  are indicated by the arrows. The fit to the low-temperature zero-field data with eqn (S13) (ESI<sup>†</sup>) is shown in green, and the contribution from the nuclear Schottky is shown as a dotted grey line. The data from Muro *et al.*<sup>8</sup> on polycrystalline samples are included for comparison. (b) Comparison of electronic specific heat  $C_{el}/\gamma_n T$  with BCS theory, and the self-consistent two-band Eilenberger model ("Model 3", as discussed in ESI<sup>†</sup>, S10). (c) and (d) Magnetization versus internal field, for applied fields along the *a*-axis and *c*-axis, respectively. The dotted grey lines represent the theoretical slope  $4\pi\chi_v = -1$ , in excellent agreement with the data. (e) The field-temperature phase diagram highlights the difference in the intermediate (type-I, orange) or vortex (type-II, blue) state, with normal regions in white. (f) The diamond-shaped (FS III) and ellipsoidal (FS IV) Fermi surfaces from the Dirac nodal line in the tight-binding model, shown in the  $k_z = 0$  plane.

In contrast to the high-temperature specific heat capacity, which is dominated by phonons and electrons (quantified by the Debye factor  $\beta_3$  and Sommerfeld constant  $\gamma_n$ , respectively),  $C_p(T)$  at low  $T$  is dominated by a nuclear Schottky anomaly (see ESI<sup>†</sup>, S6 for more details on the corresponding modeling). Subtracting the nuclear Schottky and phonon contributions from the measured specific heat allows us to estimate the zero-field electronic specific heat in a simplified model,  $C_{el}(T) = C_p(T) - C_N(T) - \beta_3 T^3$ , shown in Fig. 3b. From these data, we conclude that superconductivity in LaCuSb<sub>2</sub> is a bulk property and not a secondary phase or surface effect. The electronic specific heat capacity also may be directly compared with predictions from BCS theory. For instance, the size of the specific heat jump in zero field  $\Delta C/\gamma_n T_c = 0.94(4)$  is less than that expected from BCS theory of  $\Delta C/\gamma_n T_c = 1.43$ . Furthermore, the electronic specific heat features an abrupt drop at low temperatures near  $T^* \approx 0.35$  K, resulting in an exponentially-activated low  $T$  regime. This anomaly is present in both the total specific heat (Fig. 3a) and the electronic specific heat



(Fig. 3b), and occurs at a similar temperature to the kink in the high-pressure susceptibility data in Fig. 2c. Such feature is consistent with multigap superconductivity, a natural consequence in this multiband metal. We explore several possible models in the ESI,<sup>†</sup> S10, including the Eilenberger self-consistent two band model,<sup>12</sup> shown in Fig. 3b.

## 2.5 Quantum oscillations

For experimental information about the Fermi surface for a stoichiometric sample, we studied quantum oscillations in the Hall resistivity for which the oscillation strength is the largest. The large room temperature to residual resistivity ratio of 16.1(2) indicates high sample quality (see ESI,<sup>†</sup> S4). The magnetoresistance  $\rho(H)/\rho(0)$  is nearly linear in fields up to 16 T (Fig. 4a), and is largest at the lowest temperatures, similar to previous results found for this Dirac material.<sup>6</sup> The Hall data (Fig. 4b) show nearly linear behavior for fields less than 7 T, but is non-linear and display quantum oscillations for fields between 7 T and up to the highest fields measured (16 T). We extracted the oscillatory behavior as a function of field and temperature from the Hall data (Fig. 4c). Using the amplitude of the  $\nu = 48$  T oscillation and the Lifshitz–Kosevich formula,<sup>13</sup> we extracted an effective mass of  $m_a^* = 0.058 m_c$  for the corresponding charge carriers (Fig. 4d), which are associated with small electron pockets near the X point. Both the oscillation frequency  $\nu$  and the effective mass  $m_a^*$  is within error bar of earlier measurements in samples from Chamorro *et al.*<sup>6</sup> and Akiba *et al.*,<sup>14</sup> which indicates that self-doping has negligible effects on the extremal dimensions of the Fermi surface. Lastly, we note any splitting of Dirac to Weyl nodes would require Zeeman shift from large magnetic fields (order of  $\sim 10$  T and higher), so we would not expect to be able to discern an

anomalous Hall effect at low fields near the regime of the superconducting critical fields (order of  $\sim 100$  Oe). Furthermore, we expect any potential signatures suggestive of the chiral anomaly will be obfuscated by the multi-band nature which can make it difficult to unambiguously relate it to the non-trivial character of the Dirac bands.

## 2.6 Anisotropic magnetization

We turn to magnetization measurements on the optimized sample to study the superconducting critical fields. Demagnetization corrections were taken into account to allow us to report the internal magnetic field  $H_{\text{int}}$  (see ESI,<sup>†</sup> S3). Fig. 3c and d shows the demagnetization-corrected magnetization data for internal fields along the *a*- and *c*-axis, respectively. Note the slopes  $\chi = dM/dH_{\text{int}}$  are consistent with the expected value for bulk superconducting susceptibility  $4\pi\chi = -1$  in both cases. With applied fields along the *a*-axis, the magnetization is linear at small fields indicative of a Meissner state, but then the diamagnetic magnetization gradually decreases for  $H > H_{c1}(T)$ , suggestive of the development of a vortex state. A small critical field  $H_{c2}(0) = 172(6)$  Oe is deduced by extrapolating the magnetization data to zero temperature (see ESI,<sup>†</sup> S3). For applied fields along the *c*-axis, the magnetization remains linear over an extended field range until it sharply drops to zero magnetization near a critical field, in contrast to the gradual decay for  $H||a$ . While not definitive on their own, these data hint at distinct superconducting responses in different magnetic field orientations, sketched in Fig. 3e.

## 2.7 Transverse-field $\mu\text{SR}$

We confirm the unusual nature of the response to applied fields in sample-averaged thermodynamic measurements using with muon spin rotation ( $\mu\text{SR}$ ) measurements. Specifically we used transverse-field (TF)  $\mu\text{SR}$  to measure the distribution of internal field at muon stopping sites as a function of applied fields along the *a* and *c* directions. The geometry of the experiment is shown in Fig. 5a, with the co-mounted samples shown in Fig. 5b. When the samples were co-aligned with the magnetic field parallel to the *a*-axis, the real Fourier transform amplitude (Fig. 5d) of the asymmetry data (Fig. 5c) shows a broad peak centered at fields lower than the applied field. The broad distribution of internal fields sampled by the muon ensemble indicates the formation of a vortex lattice. We fit the asymmetry data to

$$A_a(t) = A_0 [F e^{-\sigma^2 t^2/2} \cos(\omega t + \phi) + (1 - F) e^{-\lambda_{\text{bg}} t} \cos(\omega_{\text{bg}} t + \phi)] \quad (1)$$

here  $F$  is the fraction of muons that stop in  $\text{LaCuSb}_2$  with the remainder stopping in the Ag sample holder.  $\omega = \gamma_{\mu} H_{\text{int}}$  is the muon precession frequency in the average internal field;  $\omega_{\text{bg}} = \gamma_{\mu} H_{\text{app}}$  is the corresponding frequency for muons that stop in the silver sample holder.  $\lambda_{\text{bg}}$  describes the exponential relaxation rate for muons that stop in Ag.  $\sigma$  characterizes the width of the internal field distribution in the sample.  $\gamma_{\mu} = 2\pi 135.5 \text{ MHz T}^{-1}$  is the gyromagnetic ratio of the muon and  $\phi$  is the phase angle of the initial muon polarization. For the

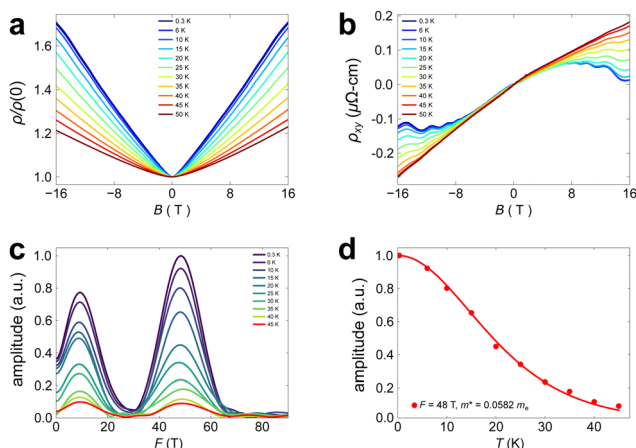


Fig. 4 Quantum oscillations for *c*-axis oriented magnetic fields in the optimal  $N_{\text{Cu}} = 2$   $\text{LaCuSb}_2$  samples. (a) Magnetoresistance  $\rho(H)/\rho(0)$  at various temperatures from 0.3 K to 50 K and for applied magnetic fields up to 16 T. (b) Hall effect for fields up to 16 T, showing nonlinearity and quantum oscillations in high fields. (c) Amplitude of the quantum oscillations as a function of frequency, for various temperatures. Note the peak near 10 T may be an artifact of the background removal. (d) Amplitude of the 48 T peak as a function of temperature, fit with the Lifshitz–Kosevich formula to extract the effective cyclotron mass.





**Fig. 5** Transverse-field  $\mu$ SR investigation on  $\text{LaCuSb}_2$ . (a) Experimental set-up for the  $\mu$ SR experiment. The muon spin is flipped to be perpendicular to the incident beam, and the magnetic field  $H_{\text{app}}$  is applied horizontally. The left/right detectors were used for the experiment. (b) Image of the co-mounted samples mounted with the  $a$ -axis out of the page (in the same direction as  $H_{\text{app}}$ ) and with the  $c$ -axis horizontal. (c) Muon asymmetry and (d) real Fourier amplitude in the type-II superconducting state for  $H_{\text{app}} \approx 40$  Oe applied along the  $a$ -axis. There are peaks at the applied field, and smaller internal fields experienced by the muons in the vortex state. Solid lines are fits to eqn (1). (e) Muon asymmetry and (f) real Fourier amplitude in the type-I superconducting state for  $H_{\text{app}} \approx 40$  Oe applied along the  $c$ -axis. There are peaks at the applied field, and a larger internal field experienced by the muons in normal regions. Solid lines are fits to eqn (2).

purpose of our analysis, the Gaussian relaxation term in eqn (1) provides an adequate approximation to the Fourier transform of the internal field distribution  $n(H)$  for the vortex lattice, which peaks at fields  $H < H_{\text{app}}$ .<sup>15</sup> With certain assumptions (see ESI,† S8), we used the temperature dependence of the relaxation rate to obtain the superfluid density  $\rho(T) = \lambda^2(0)/\lambda^2(T)$ . This may be compared to theoretical models to extract information about the gap function, and possible multiband effects. Most notably, we find the low temperature limit is consistent with conventional  $s$ -wave behavior and no thermal anomaly is observed in  $\rho(T)$  near  $T^*$  (see Fig. S8 for a more detailed discussion of the fitting models, ESI†).

Our measurements with the magnetic field along the  $c$ -axis are in stark contrast to the previous case. The real Fourier transform amplitude (Fig. 5f) of the asymmetry data (Fig. 5e) featured a broad peak at internal fields higher than the applied field. To understand this, we note that in the Meissner state, most muons will enter the superconductor where  $B = 0$ , while muons implanted in the Ag sample holder precess in the applied field. However, due to demagnetization effects, some regions of the superconducting sample sustain an internal field that is greater than the critical field  $H_c$ . In type-I

superconductors, such a region must become normal, as there is no other state (such as a vortex state) to support superconductivity. A type-I superconductor with demagnetization factor  $N$  in an applied field  $H_{\text{app}} > (1 - N)H_c$  is in the intermediate state, characterized by laminar structures of superconducting and normal regions, the latter of which maintains a constant internal field equal to the critical field  $H_c$ .<sup>16,17</sup> In our  $\mu$ SR experiment,  $N \approx 0.86$  for the plate-like ensemble of co-aligned single crystals, and  $H_c(0) = 59.8(1.0)$  Oe from fits to magnetization data, meaning that in applied magnetic fields above  $H_{\text{app}} \approx 8.4$  Oe, the samples were assuredly in the intermediate state. Therefore, the observed oscillation frequency in the  $\mu$ SR spectrum corresponds to the critical field  $H_c$ . To model the data and extract  $H_c(T)$ , we fit the asymmetry spectrum using the equation

$$A_c(t) = A_0[F(1 - F_S)e^{-\sigma^2 t^2/2} \cos(\omega t + \phi) + (1 - F)e^{-\lambda_{\text{bg}} t} \cos(\omega_{\text{bg}} t + \phi)] \quad (2)$$

here  $F$  as before is the fraction of muons stopping in the sample, and  $F_S$  is the superconducting volume fraction of that sample. Only the normal regions with volume fraction  $F(1 - F_S)$  will have a non-zero frequency  $\omega$  due to the intermediate state. From the fits to the data, we find a large superconducting volume fraction  $F_S = 0.924$  at 20 mK and 10 Oe, indicative of a bulk superconductor and consistent with the thermodynamic data. We also extracted the critical field  $H_c(T)$  by tracking the temperature-dependence of the frequency  $\omega > \omega_{\text{bg}}$  from the normal regions in the sample. We found that for  $T \in [0.02, 1]$  K and in applied fields of 10 Oe and 40 Oe, the FFT spectrum of muon precession always showed a peak at a field higher than the applied field. Combining the data in  $a$ -axis and  $c$ -axis oriented magnetic fields allows us to map out the phase diagram, with the vortex behavior (and lack thereof) sketched in Fig. 3e and shown quantitatively in Fig. S9 (ESI†). Overall, these results provide microscopic evidence that  $\text{LaCuSb}_2$  is in a type-I superconducting intermediate state when magnetic fields are applied parallel to the  $c$ -axis, and type-II superconducting state when magnetic fields are applied parallel to the  $a$ -axis, confirming the possibility from the bulk thermodynamic data.

## 2.8 Tight-binding model and superconductivity

The exponentially-activated specific heat capacity at lowest temperatures without a residual Sommerfeld coefficient indicates the entire Fermi-surface is gapped. However, few experimental probes are sensitive to discern superconducting quantities for each of the four Fermi surfaces (FS) separately. To find additional impacts of the Dirac bands on superconductivity in  $\text{LaCuSb}_2$ , we implemented a tight-binding model for the multiple bands associated with Sb orbitals as dictated by space-group symmetry.<sup>5,18</sup> The derivation is described in detail in ESI,† S9. The modeled Fermi surfaces (shown in Fig. 3f, see also Ruszala *et al.*<sup>19</sup>) are the quasi-two-dimensional diamond-shaped nodal lines, and the small ellipsoidal pockets whose orbits are observed in the quantum oscillations. These FS arise from the same band in the extended zone scheme and are highly anisotropic, in line with the observed anisotropic superconducting



quantities (further quantified in the discussion section and ESI†, S5). The anisotropic Sb Fermi surfaces contrast with the more three-dimensional Fermi surfaces derived from Cu and Sb orbitals near the  $\Gamma$  point, the latter of which we do not model due to a lack of microscopic parameters for a tight-binding model. The pair-wise degeneracy of the Dirac bands at  $X$  is enforced by the nonsymmorphic symmetry of the space group. These bands intertwine across the Brillouin zone, which contributes additional spin-orbital texture to bands near the  $X$  point. From the superconducting fitness method,<sup>20</sup> we predict that the most general gap function on the Dirac nodal lines has in-plane anisotropy,  $\Delta(k) \sim \Delta_1 + \Delta_2(\cos k_x + \cos k_y)$ . This gap anisotropy is generic and independent of the chemical potential, arising instead from the existence of Dirac bands whose bandwidths exceed several hundred millielectronvolts. We cannot resolve this anisotropy with our thermodynamic probes, but the anisotropy may impact the sensitivity of the superconductivity to disorder.

### 3 Discussion

Despite the experimentally observed anisotropy, we gain quantitative insight into the superconducting state by calculating thermodynamic quantities in a one-band, isotropic free-electron model as a first approximation. The relevant thermodynamic and superconducting quantities are tabulated in Table S5 (ESI†). In particular, we find a coherence length of  $\xi \approx 1 \mu\text{m}$ , whereas the mean-free path is  $\ell \approx 0.06 \mu\text{m}$ . This suggests LaCuSb<sub>2</sub> is in the dirty limit<sup>21</sup> since  $\xi \gg \ell$ . The relevant expression<sup>22</sup> for calculating the Ginzburg-Landau (GL) parameter in the dirty limit is  $\kappa = (7.49 \times 10^3) \gamma_{nV}^{1/2} \rho_0$  (with all quantities in cgs units), where  $\rho_0$  is the value of the low-temperature residual resistivity plateau. The out-of-plane GL parameter  $\kappa_c$  depends on currents generated in the  $ab$  plane, so using  $\rho = \rho_{0a}$  for in-plane resistivity, we find  $\kappa_c = 0.398(7)$ . That  $\kappa_c < 1/\sqrt{2}$  is consistent with type-I superconductivity for  $H||c$ . Extrapolating our magnetization data to  $T = 0$ , we have  $H_c = 59.8(1.0)$  Oe and  $H_{c2} = 172(6)$  Oe and thereby estimate<sup>21</sup>  $\kappa_a = H_{c2}/\sqrt{2}H_c = 2.03(8)$ . Next, we use conventional BCS theory to estimate the thermodynamic critical field  $H_c$ . This field is related to the gap function and density of states,<sup>23</sup> and in cgs units is given by  $H_c(0) = 1.764\sqrt{6/\pi} \cdot \gamma_{nV}^{1/2} T_c$ . From this we estimate that  $H_c(0) \approx 68(1)$  Oe, in remarkable agreement with the measured phase diagram (see Fig. S9, ESI†).

Although type-I superconductivity is mainly found in elemental superconductors and several binary compounds (e.g. noncentrosymmetric BeAu<sup>16</sup> and Dirac semimetal candidate PdTe<sub>2</sub><sup>24</sup>), it has also been observed in ternary compounds including LaRhSi<sub>3</sub><sup>25</sup> and LiPd<sub>2</sub>Ge,<sup>26</sup> among others. Furthermore, it is at the same time possible to satisfy that  $\kappa_c < 1/\sqrt{2}$  and  $\kappa_a > 1/\sqrt{2}$  when the anisotropy factor<sup>27,28</sup>  $\gamma \equiv \kappa_a/\kappa_c \gg 1$ , implying a superconductor whose type depends on the applied magnetic field direction.<sup>27,29,30</sup> In particular, the direction of the field relative to the crystallographic axes will either favor or disfavor vortices in the superconducting order parameter,

based on the free energy in distinct crystallographic directions. While rare, this behavior has been observed in C<sub>8</sub>K<sup>31</sup> and TaN,<sup>22,32</sup> where the angular dependence of the critical field was explicitly studied. However, such an anisotropy seems not to be well-studied in ternary systems.

Using DFT calculations (as shown in ESI† 5 and Table S4, ESI†), we deduce that the main contribution to the type-I/type-II anisotropy in LaCuSb<sub>2</sub> is the Dirac band structure. From semiclassical transport theory,<sup>33</sup> the conductivity is related to the squared Fermi surface velocity from each band  $\sigma_a \sim \sum_n \langle v_{a,n}^2 \rangle$ , but has dominant contribution (about 80%) from the Dirac diamond nodal line. Furthermore, in the dirty limit, the large in-plane conductivity  $\sigma_a = 1/\rho_a \sim 1/\kappa_c$  results in small in-plane GL parameter  $\kappa_c$  for out-of-plane fields. Thus, the Dirac character of the bands, with small in-plane effective masses and relativistic Fermi surface velocity, yields the small  $\kappa_c$  that engenders type-I superconductivity. Concomitantly, the type-II behavior arises from the quasi-two-dimensionality of the Dirac diamond nodal line. The anisotropy factor in dirty one-band superconductors is related to the anisotropic Fermi velocities as  $\gamma^2 = \langle v_a^2 \rangle / \langle v_c^2 \rangle$ . Namely, the anisotropy of the GL parameter is directly related to the anisotropy of the Fermi surface. Considering the previous estimates of  $\kappa_a$  and  $\kappa_c$ , the large anisotropy parameter  $\gamma^2 \approx 26(2)$  is easily explained by the highly-two-dimensional diamond-shaped Dirac nodal line. This Fermi surface has an estimated anisotropy factor of  $\gamma^2 = 18.6$  stemming from the large effective mass along the  $c$ -axis, and therefore dominates this anisotropic response, compared to the more three-dimensional trivial bands. (In the full multiband consideration, the ratios are weighted by the density of states and gap size, the latter of which we do not estimate by density functional theory.) In summary, the Dirac bands and their anisotropy directly impact the anisotropy in the magnetic field response to the superconductivity.

The fact that  $N_{\text{Cu}}$  can tune a wide range of compositions is likely due to the change of thermodynamic chemical potential and stable phases that can emerge in the LaCu<sub>x</sub>Sb<sub>2</sub> solid-solution-type structure. If the main role of the Cu off-stoichiometry is interpreted as the introduction of non-magnetic impurities (as opposed to stacking defects, see TEM results below), in the form of vacancies or interstitial sites, then according to Anderson's theorem on dirty  $s$ -wave superconductors, such defects should have no effect on  $T_c$ .<sup>34</sup> There may be several ways to reconcile this. One possibility is that the small effects of off-stoichiometry may be affecting the Fermi level and density of states, as suggested in resistivity measurements (see ESI†, S4), thereby resulting in stronger dependence of  $T_c$  as expected under conventional BCS theory.<sup>21</sup> Another possible explanation is that the gap function itself is anisotropic leading to strong dependence of  $T_c$  on the scattering rate, a well-known result from Gor'kov.<sup>35,36</sup> Indeed, an anisotropic gap function is expected from our tight-binding model for the pairing gap function. It is possible that one or both effects could explain the drastic suppression of  $T_c$  with doping and pressure. Thus, the presence of Dirac bands naturally explains the sensitivity to non-magnetic disorder *via* anisotropic band gap, in addition to



the extreme anisotropy in the response to an applied magnetic field. Overall, despite the fragility of the superconducting state in LaCuSb<sub>2</sub> to stoichiometry, pressure, and magnetic fields, it is worth exploring related compounds, perhaps ones that contain magnetic moments, to continue the search for exotic superconducting phases.

## 4 Author contributions

Sample synthesis and data analysis on the superconducting state was performed by C. J. L. under the supervision of C. L. B. and T. M. M. The  $\mu$ SR experiments were carried out by C. J. L., J. G., M. P., S. S., and P. O. under the supervision of C. L. B. and G. M. L. The tight-binding analysis was performed by J. Z. under the supervision of Y. L. The DFT calculations for the band structure were performed by S. G. The heat capacity measurements were performed by C. J. L. and T. H. The He3 susceptibility and magnetization measurements were performed by C. J. L., T. B. and J. R. C. Quantum oscillations were measured and analyzed by G. G. under the supervision of B. J. R. Single-crystal X-ray diffraction measurements and refinements were performed by M. A. S. TEM measurements were performed by K. J. T. L. The hydrostatic pressure measurements were performed by K. M. and D. K. B. under the supervision of Y. U. and S. N. All authors contributed with comments and edits.

## 5 Methods

### 5.1 Synthesis

Single crystals of LaCuSb<sub>2</sub> were grown by the self-flux method. Cut pieces from lanthanum ingot (Ames Laboratory, 99.99%), pieces of copper (Alfa Aesar, 99.999%), and antimony shot (Strem Chemicals, 99.9999%) were weighed with a total mass of about 4 g in various molar ratios and placed in an alumina crucible. An inverted catch crucible with an alumina strainer was placed atop the first crucible, and both were sealed in a quartz tube under partial pressure of argon gas. The ampules were heated to 1070 °C at a rate of 100 °C h<sup>-1</sup> and held for 12 h, then cooled to 670 °C at a rate of 4 °C h<sup>-1</sup> before centrifuging. Inspired by previous literature on isostructural LaAgSb<sub>2</sub>, which was reported to produce stoichiometric samples with starting ratio 0.045:0.091:0.864 (or roughly, 1:2:19.2),<sup>37,38</sup> we used varying compositions 1:*N*<sub>Cu</sub>:19.2 with 1 ≤ *N*<sub>Cu</sub> ≤ 6 as a parameter to tune the chemical potential of the system and grow crystals with different Cu content.

Polycrystalline samples were also prepared using a simple reaction of the elements in a quartz tube. Powders with ratios 1:δ:2 with δ = 0.8, 1.0, 1.2 were synthesized by first melting about 1.0 g of the elements in a quartz tube, using a step furnace at 600 °C for 24 hours. This polycrystal was then ground and reheated to 800 °C for roughly 12 hours. Further heating of the powder at high temperatures, or low temperatures for extended periods of time, was disadvantageous due to the decomposition of the structure, as evidenced by larger relative percentages of secondary phases Sb and Cu<sub>2</sub>Sb. We compared

the lattice constants (in particular, the *c/a* ratio) of the polycrystalline samples to those of our single crystals, and to those from the literature.

### 5.2 X-ray diffraction

Powder XRD data were collected at room temperature using a laboratory Bruker D8 Venture Focus diffractometer with LynxEye detector in the range from 10–80 degrees. Refinements on the powder XRD data were performed using Topas 5.0 (Bruker). The occupancy of La and Sb ions were constrained to 100%, while the Cu occupancy was refined freely. We also refined the strain parameter and preferred orientation, due to the layered nature of the crystals.

Single-crystal XRD data were acquired at 110(2) K using a SuperNova diffractometer (equipped with Atlas detector) with Mo K $\alpha$  radiation ( $\lambda = 0.71073$  Å) under the program CrysAlisPro (Version CrysAlisPro 1.171.39.29c, Rigaku OD, 2017). The same program was used to refine the cell dimensions and for data reduction. The structure was solved with the program SHELXS-2018/3 and was refined on F2 with SHELXL-2018/3.<sup>39</sup> Analytical numeric absorption correction using a multifaceted crystal model was applied using CrysAlisPro. The temperature of the data collection was controlled using the system Cryojet (manufactured by Oxford Instruments). For all samples in the ZrCuSiAs structure type, the occupancy factor for Cu1 was refined freely. For samples in the defect-CaBe<sub>2</sub>Ge<sub>2</sub> structure type, the additional Cu site (denoted Cu1') was necessary to obtain good fits to the data. The occupancy factor for both Cu1 and Cu1' were refined freely, and the reported occupancy is  $x_{\text{Cu}} = x[\text{Cu1}] + x[\text{Cu1}']$ . Crystallographic data tables are included in the ESI.†

### 5.3 Specific heat

Heat capacity measurements were performed in a Quantum Design Physical Properties Measurement System (PPMS) with the dilution refrigerator option. The magnetic field was degaussed above 3.8 K to minimize effects of persistent fields. Measurements were performed on a single crystalline sample of LaCuSb<sub>2</sub> of 10.7(1) mg mass oriented such that the applied magnetic field was along the nominal *c*-axis, with reported fields depicted in Fig. 3 between 0 Oe and 75 Oe. All measurements were performed in a fixed magnetic field and measured upon cooling, with a minimum temperature between  $T = 0.05$ –0.1 K and a maximum temperature of  $T = 3.8$  K.

### 5.4 Magnetization

Magnetization measurements were performed in a Quantum Design (QD) Magnetic Properties Measurement System (MPMS) with QD iHelium3 He3-insert. To extract the superconducting dome, we measured samples with nominal applied fields of 2 Oe along the *a*-axis, after degaussing at temperatures above *T*<sub>c</sub>. The samples were cut with a large aspect ratio along the *a*-axis such that the demagnetization corrections were small. Measurements on the optimal sample were performed taking into account the non-zero demagnetization factors. We performed isothermal measurements in applied field by first degaussing at



high temperature above  $T_c$ . We then cooled in zero field to the appropriate temperature, and measured from zero to fields well past the point that magnetization vanished to study  $4\pi M$  versus  $H_{\text{int}}$ .

### 5.5 Electrical transport

Quantum oscillations of the Hall resistivity were measured in a single crystal cut from the same crystal used for other thermodynamic measurements, at temperatures down to 0.3 K and fields up to 16 T. Resistivity and Hall effect measurements above 2 K were performed on a PPMS using the AC Transport (ACT) option. For all resistivity measurements we prepared a polished bar-shaped crystal with the current applied along the  $a$ -axis, using a four-probe configuration consisting of platinum wires and Epo-Tek silver epoxy. Low-temperature resistivity measurements were performed in a PPMS using a Lake Shore Model 372 AC Resistance Bridge. We applied an AC current of 316  $\mu\text{A}$  at a frequency of 13.7 Hz. The field was applied along the  $c$ -axis after degaussing the magnet at 1.1 K (above the transition) to reduce the effect of persistent magnetic fields. Measurements were taken upon cooling in various applied fields.

### 5.6 Hydrostatic pressure

Measurements under hydrostatic pressure up to 2.0 GPa were performed using a Bluefors dilution refrigerator down to 0.05 K at the Institute for Solid State Physics (ISSP), The University of Tokyo. To track the variation of the superconducting transition temperature under hydrostatic pressure, the AC magnetic susceptibility of a sample was measured with a mutual induction method at a fixed frequency of 317 Hz with a modulation field of about 1 Oe. Measurements were performed on the optimized samples  $N_{\text{Cu}} = 2$ , cut from the same crystal used for magnetization, specific heat, and resistivity measurements. For applying pressure, a piston-cylinder cell made from nonmagnetic BeCu and NiCrAl alloys was used with Daphne 7373 as the pressure transmitting medium. The pressure was determined from the superconducting transition temperature of a Pb sample within the cell.

### 5.7 Muon spin rotation

Zero-field and transverse-field muon spin rotation and relaxation measurements were performed at the TRIUMF facility in Vancouver, Canada. A spectrometer incorporating a dilution refrigerator was used on the M15 beamline, to allow for measurements down to 20 mK. The setup makes use of a superconducting magnet to allow for magnetic fields up to 5 T, and resistive coils for finer control and field-zeroing. The magnetic field was applied horizontally, parallel to the direction of the muon beam. In the ZF measurements, the muon spin was antiparallel to the beam direction, while in TF measurements the muon spin was perpendicular to the field and beam direction. Single crystals grown with the optimal ratio  $N_{\text{Cu}} = 2$  and with the greatest thickness (average 1.0 mm) were cut along the  $a$ -axis. We used multiple co-aligned single crystals, with a total mass of 0.98(2) g, to maximize the

measured signal and reduce background from muons not implanted in LaCuSb<sub>2</sub>. The crystals were first mounted with the  $a$ -axis parallel to the applied field for the first measurement, and the same crystals were then individually rotated and remounted with the  $c$ -axis parallel to the applied field for the second measurement. The samples were mounted on a silver cold finger using a mixture of Apezion N grease and copper-loaded Cry-Con grease to ensure good thermal contact. For the field along the  $a$ -axis, we used  $H_{\text{app}} = 40$  Oe. For the field along the  $c$ -axis, we used  $H_{\text{app}} = 40$  Oe to access low critical fields and  $H_{\text{app}} = 10$  Oe to access higher critical fields. All data at constant field were simultaneously refined and fit for various temperatures using the musrfit program.<sup>40</sup>

## Note added

While writing this paper, we became aware of an experimental study on single crystals of LaCuSb<sub>2</sub>.<sup>14</sup> The specific heat, resistivity, and Hall effect measurements are consistent with our data. However, no investigation into the magnetic field anisotropy was reported. Furthermore, the presence of a low-temperature feature in thermodynamic measurements allows us to gain insight on the contributions from the Dirac band structure.

## Data availability

The data that support the findings of this study are available in the main text, ESI,† as well as from the corresponding authors upon request.

## Conflicts of interest

The authors declare that they have no competing financial interests.

## Acknowledgements

It is a great pleasure to celebrate the distinguished scientific career of Professor T. T. M. Palstra. Collin would like to thank Thom for a long-lasting scientific friendship that started with an inspiring collaboration on superconductivity and magnetism in URu<sub>2</sub>Si<sub>2</sub> at Risø and was fortified during an exciting period of discovery at Bell Labs. Congratulations Thom and best wishes! This work was supported as part of the Institute for Quantum Matter, an Energy Frontier Research Center funded by the U.S. Department of Energy, Office of Science, Office of Basic Energy Sciences, under Award DE-SC0019331. C. J. L. acknowledges the support of the William Gardner Fellowship. The <sup>3</sup>He MPMS was funded by the National Science Foundation, Division of Materials Research, Major Research Instrumentation Program, under Award 1828490. The superconducting fitness analysis was supported by the NSF CAREER grant DMR-1848349; JZ also acknowledges the support from the JHU Theoretical Interdisciplinary Physics and Astronomy Center. Research at McMaster University was supported by the Natural Sciences and Engineering Research



Council (GML). The high pressure measurements were funded by KAKENHI (no. JP19H00648), JST-Mirai Program (no. JPMJMI20A1), JST-CREST (no. JPMJCR18T3 and JPMJCR15Q5). We would like to thank Bassam Hitti and Sarah Dunsiger for their assistance during the  $\mu$ SR experiment; Lisa Pogue for her preliminary DFT work; and Yishu Wang for her assistance with resistivity measurements.

## References

- S. Jia, S.-Y. Xu and M. Z. Hasan, Weyl semimetals, Fermi arcs and chiral anomalies, *Nat. Mater.*, 2016, **15**, 1140–1144.
- T. Liang, *et al.*, Ultrahigh mobility and giant magnetoresistance in the Dirac semimetal  $\text{Cd}_3\text{As}_2$ , *Nat. Mater.*, 2015, **14**, 280–284.
- Y. Li and F. D. M. Haldane, Topological Nodal Cooper Pairing in Doped Weyl Metals, *Phys. Rev. Lett.*, 2018, **120**, 067003.
- G. Lee, M. A. Farhan, J. S. Kim and J. H. Shim, Anisotropic Dirac electronic structures of  $\text{AMnBi}_2$  (A = Sr, Ca), *Phys. Rev. B: Condens. Matter Mater. Phys.*, 2013, **87**, 245104.
- S. M. Young and C. L. Kane, Dirac semimetals in two dimensions, *Phys. Rev. Lett.*, 2015, **115**, 126803.
- J. R. Chamorro, *et al.*, Dirac fermions and possible weak antilocalization in  $\text{LaCuSb}_2$ , *APL Mater.*, 2019, **7**(12), 121108.
- N. V. Gamayunova, *et al.*, Electron-phonon interaction in ternary rare-earth copper antimonides  $\text{LaCuSb}_2$  and  $\text{La}(\text{Cu}_{0.8}\text{Ag}_{0.2})\text{Sb}_2$  probed by Yanson point-contact spectroscopy, *2017 IEEE 7th International Conference Nanomaterials: Application & Properties (NAP)*, 1–4 (2017).
- Y. Muro, N. Takeda and M. Ishikawa, Magnetic and transport properties of dense Kondo systems,  $\text{CeTSb}_2$  (T = Ni, Cu, Pd and Ag), *J. Alloys Compd.*, 1997, **257**, 23–29.
- O. Sologub, K. Hiebl, P. Rogl, H. Noël and O. Bodak, On the crystal structure and magnetic properties of the ternary rare earth compounds  $\text{RETSb}_2$  with RE = rare earth and T = Ni, Pd, Cu and Au, *J. Alloys Compd.*, 1994, **210**, 153–157.
- M. Ohta, Thermoelectric Properties of Ternary Rare-Earth Copper Antimonides  $\text{LaCu}_x\text{Sb}_2$  ( $0.9 < x < 1.3$ ), *Mater. Trans.*, 2009, **50**, 1881–1884.
- X. X. Yang, *et al.*,  $\text{RCu}_{1+x}\text{Sb}_2$  (R = La, Ce, Pr, Nd, Sm, Gd, Tb, Dy, Ho and Y) Phases with Defect  $\text{CaBe}_2\text{Ge}_2$ -Type Structure. In PRICM-5, vol. 475 of Materials Science Forum, Trans Tech Publications Ltd, 2005, pp. 861–864.
- R. Prozorov and V. G. Kogan, London penetration depth in iron-based superconductors, *Rep. Prog. Phys.*, 2011, **74**, 124505.
- D. Shoenberg, *Magnetic oscillations in metals*, Cambridge university press, 2009.
- K. Akiba and T. C. Kobayashi, Phonon-mediated superconductivity in the Sb square-net compound  $\text{LaCuSb}_2$ , *Phys. Rev. B*, 2023, **107**, 245117.
- J. E. Sonier, J. H. Brewer and R. F. Kiefl,  $\mu$ SR studies of the vortex state in type-II superconductors, *Rev. Mod. Phys.*, 2000, **72**, 769–811.
- J. Beare, *et al.*, SR and magnetometry study of the type-I superconductor  $\text{BeAu}$ , *Phys. Rev. B*, 2019, **99**, 134510.
- V. Kozhevnikov, A. Suter, T. Prokscha and C. Van Haesendonck, Experimental Study of the Magnetic Field Distribution and Shape of Domains Near the Surface of a Type-I Superconductor in the Intermediate State, *J. Supercond. Novel Magn.*, 2020, **33**, 3361–3376, DOI: [10.1007/s10948-020-05576-1](https://doi.org/10.1007/s10948-020-05576-1).
- L. M. Schoop, *et al.*, Dirac cone protected by non-symorphic symmetry and three-dimensional Dirac line node in  $\text{ZrSiS}$ , *Nat. Commun.*, 2016, **7**, 11696, DOI: [10.1038/ncomms11696](https://doi.org/10.1038/ncomms11696).
- P. Ruzsala, M. Winiarski and S.-C. Małgorzata, Dirac-like band structure of  $\text{LaTESb}_2$  (TE = Ni, Cu, and Pd) superconductors by DFT calculations, *Comput. Mater. Sci.*, 2018, **154**, 106–110.
- A. Ramires, D. F. Agterberg and M. Sgrist, Tailoring  $T_c$  by symmetry principles: the concept of superconducting fitness, *Phys. Rev. B*, 2018, **98**, 024501.
- M. Tinkham, *Introduction to Superconductivity*. Dover Books on Physics Series, Dover Publications, 2004, <https://books.google.com/books?id=VpUk3NfwDlkC>.
- H. W. Weber, J. F. Sporna and E. Seidl, Transition from Type-II to Type-I Superconductivity with Magnetic Field Direction, *Phys. Rev. Lett.*, 1978, **41**, 1502–1506.
- N. Itoh, Superconducting state of neutron stars, *Prog. Theor. Phys.*, 1969, **42**, 1478–1479.
- H. Leng, J.-C. Orain, A. Amato, Y. K. Huang and A. de Visser, Type-I superconductivity in the Dirac semimetal  $\text{PdTe}_2$  probed by SR, *Phys. Rev. B*, 2019, **100**, 224501.
- V. K. Anand, *et al.*, Specific heat and SR study on the noncentrosymmetric superconductor  $\text{LaRhSi}_3$ , *Phys. Rev. B: Condens. Matter Mater. Phys.*, 2011, **83**, 064522.
- K. Górnicka, *et al.*, Soft-mode enhanced type-I superconductivity in  $\text{LiPd}_2\text{Ge}$ , *Phys. Rev. B*, 2020, **102**, 024507.
- R. Klemm, *Layered Superconductors: Volume 1. International Series of Monographs on Physics*, OUP Oxford, 2012, <https://books.google.com/books?id=EWORhjhzdqMC>.
- V. G. Kogan, Macroscopic anisotropy in superconductors with anisotropic gaps, *Phys. Rev. B: Condens. Matter Mater. Phys.*, 2002, **66**, 020509.
- D. Liarte, M. Transtrum and J. Sethna, Ginzburg-Landau theory of the superheating field anisotropy of layered superconductors, *Phys. Rev. B*, 2016, **94**, 144504.
- V. G. Kogan and R. Prozorov, Anisotropic criteria for the type of superconductivity, *Phys. Rev. B: Condens. Matter Mater. Phys.*, 2014, **90**, 054516.
- Y. Koike, S. Tanuma, H. Suematsu and K. Higuchi, Superconductivity in the graphite-potassium intercalation compound  $\text{C}_8\text{K}$ , *J. Phys. Chem. Solids*, 1980, **41**, 1111–1118.
- J. F. Sporna, E. Seidl and H. W. Weber, Anisotropy of the superconductive to normal transition in tantalum-nitrogen single crystals, *J. Low Temp. Phys.*, 1979, **37**, 639–661, DOI: [10.1007/BF00113876](https://doi.org/10.1007/BF00113876).
- N. Ashcroft and N. Mermin, *Solid State Physics*, Holt, Rinehart and Winston, 1976, <https://books.google.com/books?id=OXIFAQAAMAJ>.
- P. W. Anderson, Theory of dirty superconductors, *J. Phys. Chem. Solids*, 1959, **11**, 26–30.



- 35 C. Petrovic, S. L. Bud'ko, V. G. Kogan and P. C. Canfield, Effects of La substitution on the superconducting state of CeCoIn<sub>5</sub>, *Phys. Rev. B: Condens. Matter Mater. Phys.*, 2002, **66**, 054534.
- 36 L. Gor'kov and T. Melik-Barkhudarov, Microscopic derivation of the Ginzburg-Landau equations for an anisotropic superconductor, *J. Exp. Theor. Phys.*, 1964, **18**(4), 1031.
- 37 K. Myers, *et al.*, Systematic study of anisotropic transport and magnetic properties of RAgSb<sub>2</sub> (R = Y, La-Nd, Sm, Gd-Tm), *J. Magn. Magn. Mater.*, 1999, **205**, 27–52.
- 38 S. Masubuchi, *et al.*, Chemical Substitution Effect on CDW State in LaAgSb<sub>2</sub>, in *Proceedings of the International Conference on Strongly Correlated Electron Systems (SCES2013)*, **011053** (2014).
- 39 G. M. Sheldrick, SHELXT-Integrated space-group and crystal-structure determination, *Acta Crystallogr., Sect. A: Found. Adv.*, 2015, **71**, 3–8.
- 40 A. Suter and B. Wojek, Musrfit: a free platform-independent framework for  $\mu$ SR data analysis, *Phys. Procedia*, 2012, **30**, 69–73.

